

Many-body potentials of an open shell atom: Spectroscopy of spin-orbit transitions of iodine in crystalline Xe and Kr

W. G. Lawrence^{a)} and V. A. Apkarian

Department of Chemistry, Institute of Surface and Interface Science, University of California, Irvine, California 92717

(Received 3 November 1993; accepted 14 April 1994)

Temperature dependent emission spectra of spin excited iodine in crystalline Xe and Kr are presented and analyzed in terms of nonadditive anisotropic pair interactions. In the octahedral trap site, the atomic 2P states split into $E_{1/2}$ and $G_{3/2}$ groups of the double valued representation. The fourfold degenerate $G_{3/2}$ state is subject to strong Jahn-Teller instability and further splits by coupling to phonons into $E_{1/2}$ and $E_{3/2}$ Kramers pairs. Accordingly, the observed emission spectra are composed of two bands: $2E_{1/2} \rightarrow 1E_{1/2}$ and $2E_{1/2} \rightarrow E_{3/2}$ transitions. Two pairs of bands are observed each in Xe and Kr. The long-lived pairs (at 15 K, $\tau=250 \mu\text{s}$ and $930 \mu\text{s}$ in Xe and Kr, respectively) are assigned to the isolated atom, while a short lived pair of bands (at 15 K, $\tau < 1 \mu\text{s}$ in Xe, and $\tau=2.2 \mu\text{s}$ in Kr) are assigned to I atoms trapped as nearest neighbor to a localized charge, identified as $(\text{HRg})^+$. The isolated atom spectra are simulated by Monte Carlo methods which assume classical statistics in the heavy atom coordinates, and adiabatic following of the electronic coordinate. Angle dependent, gas phase pair interactions are used as a starting point. Minor modifications to the pair interactions, and a temperature dependent spin-orbit splitting constant, adequately reproduce the experimental spectra. Many-body contributions to the effective pair potentials can be estimated to change pair parameters by less than $\sim 3\%$.

I. INTRODUCTION

The many-body potentials of open shell species—atoms, radicals or molecules—as encountered in condensed media, cannot be described by simply additive radial functions.¹ Yet, for the sake of convenience, pairwise additive radial functions are commonly used to describe interaction potentials, and to treat dynamics in such systems. We have in mind the significant literature on molecular dynamics simulations of open shell systems in solids and liquids.² A notable exception to this generalization is the recent treatment of photodissociation dynamics in solids including nonadiabatic effects by Gersonde and Gabriel, in which angularly anisotropic potentials are explicitly taken into account.³ Even in the case of adiabatic dynamics, as would be expected to prevail at thermal cryogenic energies, nonadditivity of potentials are necessary to take into account, to rationalize energetics, spectroscopy, or diffusion dynamics of open shell systems in condensed media. Such applications are the motivation behind the test of simple, yet systematic approaches for the incorporation of anisotropic pair potentials with a proper account of nonadditivity, which is the aim of the present work. In this paper we consider the simplest possible test case, namely the treatment of a halogen atom trapped in a host consisting of closed shell rare gas atoms. In particular, we consider the ground state potential energy surfaces of atomic iodine isolated in crystalline Xe and Kr, and calibrate our treatment by comparing simulations of the $I^*(^2P_{1/2}) \rightarrow I(^2P_{3/2})$ transition with experiment. The many-body potential energy surfaces, including spin-orbit coupling, are constructed from the X-Rg pair interactions as determined

from gas phase scattering⁴ and spectroscopic data.⁵ The method, which relies on degenerate perturbation theory, has been adopted from classical treatments of scattering between open shell and closed shell atoms.^{1,6-9} Of particular relevance for the present is the discussion by Baylis,¹ and the implementation by Balling and Wright,¹⁰ who have considered the interactions of excited (2P) alkali atom many rare gas atoms, in terms of atom-atom pair interactions. The spectral simulation relies on the classical Franck-Condon principle, even though transitions near conical intersections of Jahn-Teller split states are being treated. A rather similar treatment has also been independently advanced by Boatz and Fajardo for the treatment of absorption spectra of alkali atoms trapped in rare gas matrices.¹¹ Extension of the present treatment to the two-electron system of O trapped in Kr and Xe crystals, in which the site specific spectra have been successfully reproduced, has already been reported.¹²

To clarify what we mean by nonadditive adiabatic many-body potentials, consider the interaction of a P atom ($l=1$) with a closed shell S atom ($l=0$). The interaction potential between the pair is a function of \mathbf{R}_{21} and θ , as defined in Fig. 1. Two eigenstates arise in this case, which in the two-center representation is referred to as V_Σ and V_Π , which define the orientation of the electron on the open shell atom relative to the internuclear coordinate. Assuming that V_Σ is the lowest eigenstate, then in the ground state the electron reorients such that $\theta=0$ [illustrated in Fig. 1(b)]. In this state, the force exerted on atom 2 by the open shell atom, atom 1, is given as $\mathbf{F}_{12} = -dV_\Sigma/dR$ which acts along $\mathbf{R}_{12}/|\mathbf{R}_{12}|$. Now consider introducing a third atom, the closed shell atom 3. To assume the ground state, the electron on atom 1 reorients, see Fig. 1(c). Accordingly, \mathbf{F}_{12} changes:

$$\mathbf{F}_{12} = -d[\alpha V_\Sigma(R_{1,2}) + \beta V_\Pi(R_{1,2})]/dR$$

^{a)}Present address, Department of Chemistry, Emory University, Atlanta, Georgia.

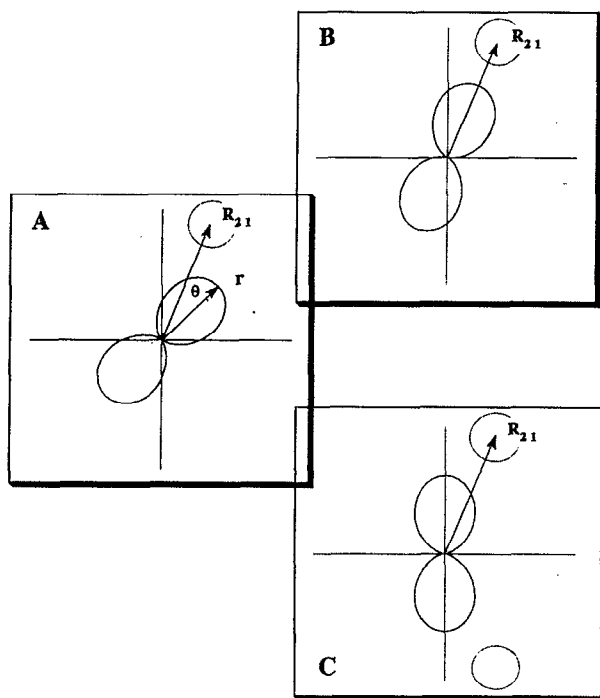


FIG. 1. Nonadditivity of many-body potentials of open shell systems. (a) The interaction of an open shell, $l=1$, atom with a closed shell atom is a function of \mathbf{R} and θ , in which θ is the angle between internuclear vector \mathbf{R} and the electronic coordinate \mathbf{r} . (b) In the lowest eigenstate, the system may be in the Σ state, in which $\theta=0$; (c) Upon introduction of a third atom in the field, the electron on 1 reorients to assume the lowest eigenstate, thus changing the 1-2 interaction energy.

acting along the same direction. The coefficients α and β are a function of positions of all atoms: \mathbf{R}_1 , \mathbf{R}_2 , and \mathbf{R}_3 . Clearly, the force exerted by atom 1 on atom 2, depends also on the position of atom 3. More generally, in a many-body system, $V_{ij} = V(r; R_1, R_2, \dots, R_n)$. If we restrict ourselves to the limit where the electron is infinitely faster than the heavy atom motions, then the eigenstates of the system can be determined from the set $\{R_i\}$, by solving the proper secular equations. This is the limit of adiabatic following, which is the appropriate limit for an open shell atom trapped in a rare gas solid, and subject only to thermal lattice fluctuations. In effect, at all times, the electron orientation is defined by the positions of the heavy atoms. With this picture in mind, we test the extent of applicability of constructing interaction potentials based on pair interactions.

Photodissociation of HI in solid Kr and Xe, is the method used for preparing I doped polycrystalline samples. The photodissociation of HI in solid Xe has previously been advanced as a possible prototype for studying reactive dynamics in crystalline solids.^{13,14} After extensive experimentation, we have concluded that this system is less than suitable for its initially intended application.¹⁵ Complications due to dynamics via ionic channels, charge delocalization and separation, and creation of a variety of ionic centers, interfere too strongly with the direct photodissociation process.¹⁵⁻¹⁷ These findings, which may not be widely appreciated, will be commented on in Sec. III. In the case of

Xe, we expect well defined substitutional trapping of the I atoms due to the similarity of I-Xe and Xe-Xe pair potentials. In the case of Kr, a more congested substitutional trapping is to be expected. In both cases we therefore expect minor local perturbations of the solid, without any ambiguity due to multiple trapping sites, or formation of large defects.

II. EXPERIMENT

Two different techniques were used to prepare the HI doped crystalline solids. Each method produced solids which were free of cracks and defects over a different temperature range.

Xenon solids at high temperature were prepared by slow cooling of a solution of HI in liquid xenon in a three window "T"-shaped cell.¹⁴ A closed cycle helium refrigerator was used to cool the cell, and the temperature was controlled with a diode and 25 watt resistive heater. The sample was formed by slow cooling of the solution while passively maintaining a temperature gradient across the cell by heating the end opposite to the contact with the cryotip. The temperature of the cell is held constant, within 0.1 K of the freezing point of the solution for 10-16 h, to allow the solid to grow along the temperature gradient. The growth starts from a nucleation site on the cold side. Although not verified, the resulting solid has all the apparent characteristics of a single inclusion crystal. These optically nonscattering solids grow to fill the entire cell, a cylinder 1.25 cm in diameter and 4 cm in length. By recording IR spectra in the liquid and solid phase, it was verified that no zone refining occurs in the case of HI/Xe solutions at concentrations as high as 25 mM, while perfectly clear near the melting point of the solid, as the temperature is lowered, the solid cracks evidently due to stresses generated from thermal contraction. The temperature for the onset of cracking depends on the cooling rate. For cooling rates of order 2 K h^{-1} , cracks were evident at $\sim 120 \text{ K}$, and the solids became highly scattering around 100 K.

Xenon of 99.999% stated purity was used without further purification, and HI was distilled into a blackened glass bulb which was coated with halocarbon wax. To avoid contamination with I_2 , the bulb was cooled in an ice-water bath prior to the transfer of the HI to the cryocell. HI is transferred to the cell at 200 K, and sufficient xenon is immediately added to fill the entire cell with liquid. The reported high temperature experiments are from a 5.7 mM solution, which creates solids with HI/Xe ratio of $\sim 1:5000$.

Free standing polycrystalline solids of HI/Xe (1/10,000) were prepared for the low temperature studies.¹⁸ These 1 cc free standing polycrystalline solids were grown by fast deposition from a premixed gas sample onto the cold tip of a cryostat. The sample was rapidly deposited through a 1/4" tube terminated by a mold consisting of a glass tube of 1 cm \times 1 cm square cross section. The mold is placed flush against the cryotip during crystal growth, and, subsequently, retracted in vacuum. The gas mixture was deposited onto the cryotip using a low pressure regulator (Tescom). To create a seal between the mold and the cryotip the pressure is initially kept below 10 Torr. After formation of the seal, the pressure is increased from 150 to 200 Torr to rapidly grow optically clear crystals. The crystal temperature was monitored using

an Fe:Au vs chromel thermocouple embedded in the crystal. A hydrogen thermometer, welded to the cryotip, provided a secondary temperature calibration. With the cryotip temperature at 14 K, the temperature of the solid was measured to be about 40 K during growth. After a sufficiently large crystal is grown, typically 1 cc, the gas flow is shut off and the temperature of the crystal drops. The crystal shrinks away from the mold as the temperature drops, allowing facile retraction of the mold.

An excimer pumped dye laser (Lambda Physik EMG 101/F1 2001) equipped with BBO doubling crystals, was used to generate laser excitation in the range from 220 to 270 nm. Typically, fluences of less than 10 mJ/cm² in an 8 ns pulse were used.

Fluorescence from the sample was collected at right angles to the excitation path. On one side, visible spectra were recorded using a 1/4 m polychromator and an optical multichannel analyzer (OMA) equipped with a gated intensified diode array. On the other side, fluorescence was collected through a 1/4 m monochromator with either a photomultiplier tube, for lifetime measurements in the visible, or a liquid-nitrogen-cooled germanium detector, for spectral and lifetime measurements in the near infrared. The response time of the latter system was 1 μ sec. The spectral sensitivity of the monochromator/germanium detector combination was calibrated using a 3000 K blackbody source.

III. EXPERIMENTAL RESULTS

The photodissociation of HI has been followed by monitoring the growth in either I or H atom concentration with irradiation time.^{14,15} Kunttu *et al.* have followed the photodissociation of HI, among other hydrogen halides, by infrared absorption spectroscopy.^{16,17} The growth of I atom concentration, is monitored by accessing the I/Rg charge transfer excitation which leads to Stokes shifted fluorescence over the $Rg_2^+I^-(4^2\Gamma \rightarrow 1^2\Gamma)$ transition. The $Xe_2^+I^-$ emission peaks at 380 nm in solid Xe,¹⁴ while the $Kr_2^+I^-$ emission peaks at 280 nm in solid Kr.¹⁹ In Xe, the H/Xe charge transfer states can be reached at 193 nm, and lead to fluorescence at 250 nm.^{20,21} In addition to these well assigned exciplexic emissions, irradiated HI doped samples lead to strong emission bands at 550 nm in Xe and at 345 nm in Kr. Although the 550 nm band in Xe has tentatively been assigned to $Xe_2^+I^-(4^2\Gamma \rightarrow 3^2\Gamma)$,¹⁴ these additional bands may arise from ionic states that are formed during the irradiation process. The photogeneration of ions has been most directly documented by the IR studies, which show that the decay of HI absorption bands is accompanied by the growth of absorptions due to such ionic species as $(Rg_2H)^+$, $(HRgI)^+$, and $(IHI)^-$.^{16,17} The accepted mechanism for the generation of ions is the separation of charge, via delocalized charge transfer states of halogen doped rare gas solids.²² Nonexponential growth of the neutral fragments, I and H, and nonexponential decay of the HI concentration are observed, which can be ascribed to strong photoabsorption cross sections of the ionic centers, and competition of ionic channels of photodynamics with that of the neutral photodissociation process.^{15,16} It has also been shown that there is a large difference between photodissociation in matrices vs that of crystalline samples.¹⁵ In

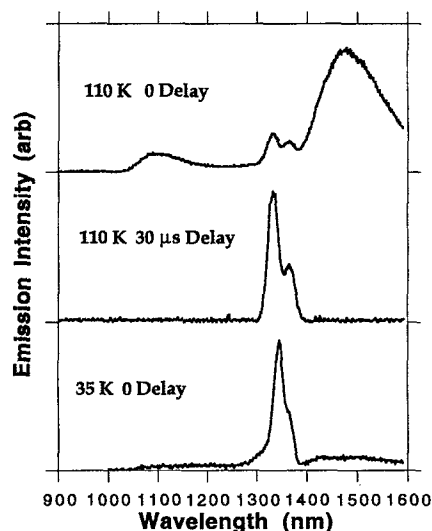


FIG. 2. Emission spectra in irradiated HI/Xe crystalline solids. The 110 K data are from a solid grown from the liquid phase. They are recorded with and without a delay gate. The top trace therefore corresponds to total emission, while the middle trace corresponds to long-lived emissions only. The 35 K data are from a free standing crystal, the short-lived emission is quite weak in this case.

matrices exponential growth of the I photoproduct is observed, with a photogeneration quantum yield that is an order of magnitude larger than that in the crystalline samples. It is suspected that this dramatic difference in efficiencies is the result of different mobilities of the H atom photofragment in the two media, and the fact that H centers act as ion traps in these solids. The fascinating energetics and photodynamics of the ionic species remains the subject of research.^{23,24} In addition to the UV-Vis emissions, charge transfer excitation of I/Rg, leads to near IR emission, near the $I(^2P_{1/2} \rightarrow ^2P_{3/2})$ spin-orbit transition which for the isolated atom occurs at 1315 nm. These transitions, which are the focus of the present study, have previously been observed in I₂ doped solids.^{25,26} We have also conducted thermal cycling studies in these solids to verify that the atomic H centers decay, presumably by diffusion and subsequent formation of H₂, at 50 K. This temperature is also near the ion-hole recombination temperature in Xe, and indeed upon heating the solids the radiative ion-hole pair recombination is observed.²² An additional thermoluminescence band at 530 nm is observed near 48 K in Xe.¹⁵ This emission is correlated in the IR studies with the formation of a strong chromophore ascribed to $(HXe)^+$.^{16,17} The near IR emission spectra are therefore obtained from samples in which beside I/Rg, charged species are present.

Excitation of a well irradiated sample of original concentration 1/10 000 HI/Xe at 280 nm produces the emission spectra shown in Fig. 2. Of the four peaks shown in the spectrum recorded at 110 K, the two center peaks at 1340 and 1360 nm decay with a lifetime of 250 μ sec, while the peaks at 1100 and 1500 nm show a detector limited lifetime: $\tau < 1 \mu$ s. The long-lived emissions can be isolated by delayed gated detection, as shown in the second trace of Fig. 2. At

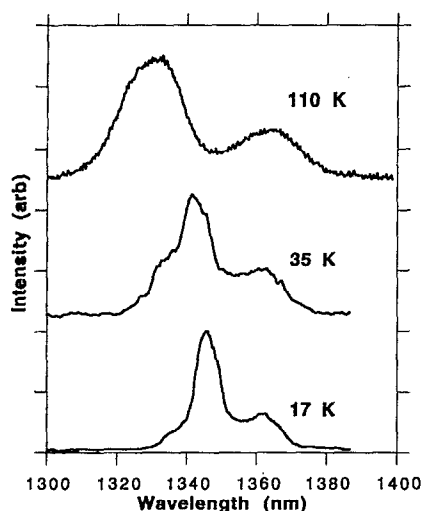


FIG. 3. Temperature dependence of the long-lived $I^* \rightarrow I$ emissions in crystalline Xe.

lower temperatures, the contribution from the fast components decrease. As an example we show in Fig. 2 an emission spectrum recorded without delay at 35 K. The broad, fast emission at 1500 nm is barely discernible. At 17 K, only the long-lived component is observable.

The temperature dependence of the long-lived emissions is shown in Fig. 3, in which spectra recorded with a gate delay of 30 μs are collected. The effect of temperature on the red peak, centered near 1360, is mainly one of broadening. The blue peak loses its substructure, broadens, and shifts by $\sim 80 \text{ cm}^{-1}$ between 17 and 110 K. The peak positions, as a function of temperature, are collected in Table I.

The ultraviolet excitation spectrum of the 1360 nm emission, obtained at discrete wavelengths between 265 and 295 nm, is shown in Fig. 4, together with the excitation spectrum of the $\text{Xe}_2^+ I^-$ emission at 380 nm. The spectra are quite similar, and correspond to the charge transfer absorption of I/Xe . The latter has previously been discussed in terms of Rydberg hole progressions.²⁷ We conclude that the near IR emission is the result of accessing the I/Xe charge transfer states. The spin excited I atom can be populated from such a state either by radiation, $\text{Xe}_2^+ I^- (4^2\Gamma \rightarrow 3^2\Gamma)$ or nonradiatively, via a crossing between the repulsive wall of the $3^2\Gamma$ potential, and the manifold of ionic states. The latter mechanism is commensurate with the observation that the intensity of these

TABLE I. Experimental parameters of $I^* \rightarrow I$ emission in Xe.

T (K)	$\tau_{\text{(long)}}^a$	λ_{fast} (nm)	λ_{slow} (nm) ^b	$\Delta(\text{cm}^{-1})^c$
110	250 μs	1097/1478	1332/1366	7435
35	610 μs		1342/1362	7406
17	950 μs		1345/1362	7380

^aGas phase radiative lifetime = 100 ms.

^bPreviously reported values: 1337 and 1357 nm in Ref. 25; 1333 nm in Ref. 26(a).

^cFree atom spin-orbit splitting = 7598 cm^{-1} .

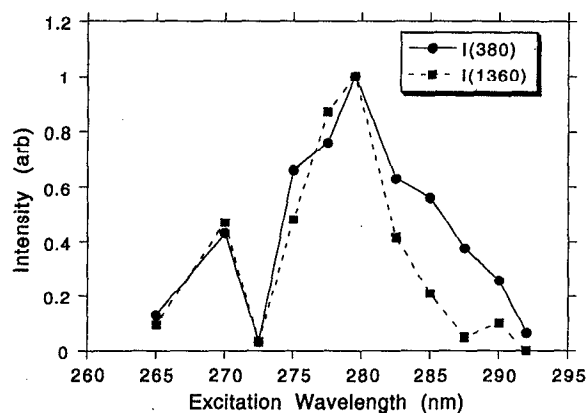


FIG. 4. Excitation profiles of the $I^* \rightarrow I$ emission (solid squares) and the $\text{Xe}_2^+ I^-$ emission (solid circles) in Xe.

near IR emissions increases as the sample temperature is raised.

Similar emissions are observed by 193 nm irradiation of HI doped crystalline krypton. Emission spectra with and without delay in a free standing crystal of krypton at 61 K is shown in Fig. 5. The histories of these emissions closely follow that of the $\text{Kr}_2^+ I^-$ emission at 280 nm ($\tau = 250 \text{ ns}$). As in the case of xenon, the near IR emissions in Kr are composed of two components: The emission at 1170 nm has a short lifetime, and the emission at 1370 nm has contributions from both long and short-lived states. The temperature dependent time profile of the fluorescence at 1370 nm is shown in Fig. 6. A fast and slow component of the lifetime are observed at all temperatures. As the temperature is decreased, the short lifetime emission becomes weaker, and the lifetime of the emission changes from 4 μs at 61 K to about 2 μs at 15 K. The lifetimes and peak positions are given in Table II. The long-lived emission, as in the case of Xe, is

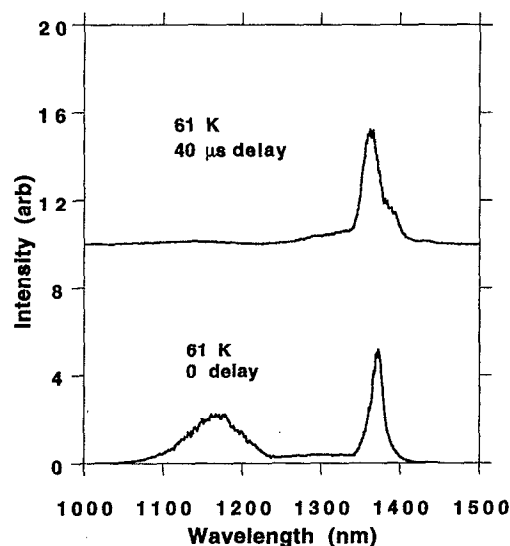


FIG. 5. $I^* \rightarrow I$ emission spectra in Kr showing both long-lived (upper trace) and total emission spectra (lower trace).

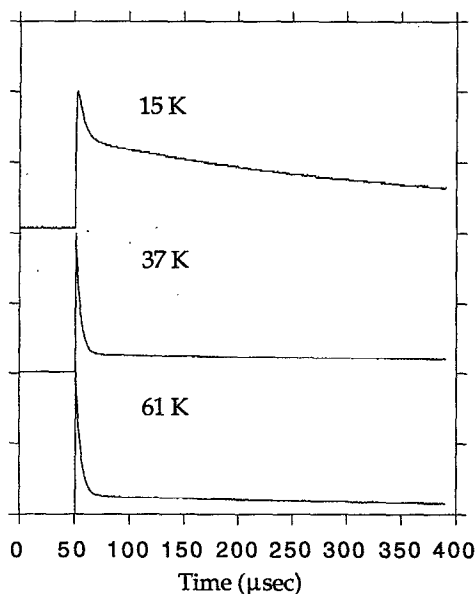


FIG. 6. Fluorescence decay curves of I^* in Kr, as a function of temperature. The decay curves are biexponential, the fast part being near the response time of the Ge detector used.

composed of two peaks which are well separated at high temperatures, see for example the 61 K spectrum in Fig. 5. As the temperature is lowered to 15 K, these peaks coalesce.

The long-lived emissions are ascribed to matrix enhanced, crystal field split $I(^2P_{1/2} \rightarrow ^2P_{3/2})$ transitions. This transition is at 1315 nm for the isolated atom, which relaxes via magnetic quadrupole radiation with a lifetime of 125 ms.²⁸ These long-lived emissions will be treated in detail in Sec. IV. We will then speculate on the origin of the short-lived emissions, as arising from open shell I atoms near a localized charge.

IV. THEORETICAL TREATMENT

A. The interaction Hamiltonian

We limit the interaction Hamiltonian of a halogen atom in the field of n closed shell rare gas atoms to:¹

$$H_{int} = V_{X-Rg}(r; R_1, R_2, \dots, R_n) + V_{Rg-Rg}(R_1, R_2, \dots, R_n) + H_{s.o.} \quad (1)$$

in which r and R represent, respectively, the coordinate of the hole and the coordinates of the rare gas atoms as measured from the origin centered on the halogen nucleus; $H_{s.o.}$ is the effective spin-orbit Hamiltonian. The hyperfine interactions are ignored except in the consideration of radiative transi-

tions. Given the large spin-orbit splitting in iodine, we expect $H_{s.o.}$ to be dominated by the hole-core coupling and only slightly modified by the lattice. Thus, the explicit dependence of $H_{s.o.}$ on $\{R_i\}$ is ignored in the development. It is also assumed that the interactions between X and Rg do not effect Rg-Rg interactions, i.e., all polarization or electron exchange effects are ignored.

The angular dependence of V_{X-Rg} can always be expanded in Legendre polynomials, P_L :

$$V_{X-Rg}(r; R_1, R_2, \dots, R_n) = \sum_{k=1}^n \sum_{l=0}^{\infty} V_L(r, R_k) P_L(\mathbf{R}_k \cdot \mathbf{r}). \quad (2)$$

The electronic eigenenergies can then be obtained by diagonalizing the Hamiltonian in the valence basis set. We are interested in the ground state of the system. Noting that the lowest excited state is the Rg^+I^- charge transfer state with energies greater than 4 eV, the limited basis set $|np\rangle_X |ns\rangle_{Rg}$, composed of the six 2P functions on the halogen atom, and the single 1S_0 function on the rare gas atoms is hoped to be adequate. Since the rare gas atoms are represented with a single ns function, they will be dropped from further explicit notation. Since the V_{X-Rg} only depends on spatial coordinates, we may first consider its evaluation in the decoupled basis set, i.e., $|lm_l, sm_s\rangle$ basis. Using the addition theorem,

$$P_L(\mathbf{R}_k \cdot \mathbf{r}) = \frac{4\pi}{2L+1} \sum_{M=-L}^L Y_{LM}(\vartheta\varphi) Y_{LM}^*(\vartheta_k\varphi_k), \quad (3)$$

in which the unsubscripted angle coordinates refer to those of the valence hole, and the subscript k is given to the electronic coordinate on the rare gas. The individual matrix elements can be expressed as products of spherical harmonics:

$$V_{mm'} = \sum_k \sum_{L=0}^{\infty} \frac{4\pi}{2L+1} \langle Y_{lm'} | \sum_{M=-L}^L Y_{LM} | Y_{lm} \rangle \times V_L Y_{LM}^*(\vartheta_k\varphi_k). \quad (4)$$

Since the basis is limited to $l=1$, the conditions $l+L+l' = \text{even}$, and $l+L+l' \geq 0$, limit the summation over L to only two terms, $L=0, 2$. The radial functions, $V_0(R)$ and $V_2(R)$ are directly extracted from pair interactions, and are related to the diatomic Σ and Π potentials:⁹

$$V_0 = \frac{1}{3}(V_{\Sigma} + 2V_{\Pi}), \quad V_2 = \frac{5}{3}(V_{\Sigma} - V_{\Pi}). \quad (5)$$

In the absence of spin-orbit coupling, and given V_0 and V_2 from either theoretical or experimental data on the pair interactions, H_{int} can be readily evaluated. The explicit expressions in polar coordinates for the individual matrix elements

TABLE II. Experimental parameters of $I^* \rightarrow I$ emission in Kr.

T (K)	$\tau_{(short)}$	$\tau_{(long)}$	λ_{fast} (nm)	λ_{slow} (nm) ^a	Δ (cm ⁻¹)
61	4.1 μ s	350 μ s	1170/1372	1362.5/1390	7250
35	3.8 μ s	1650 μ s	1168/1370	1371/1389	7220
15	2.2 μ s	930 μ s	1170/1366	1387	7210

^aPreviously reported values: 1324 and 1342 nm in in Ref. 25; 1326 nm in Ref. 26a.

in the imaginary $|lm_i\rangle$ basis set have been given previously.^{10,11} The same matrix elements in Cartesian coordinates, which are more suitable for the present treatment, are given in the Appendix.

To include the spin-orbit interaction, we note that $H_{s.o.}$ is diagonal in the $|Jm_J\rangle$ basis:

$$\langle Jm_J|H_{s.o.}|J'm'_J\rangle = \begin{cases} \frac{2}{3} \Delta \delta_{J,J'} \delta_{m_J,m'_J}, & J = \frac{1}{2}, \\ -\frac{1}{3} \Delta \delta_{J,J'} \delta_{m_J,m'_J}, & J = \frac{3}{2}, \end{cases} \quad (6)$$

in which Δ is the spin-orbit splitting in the isolated atom, $\Delta = 7606 \text{ cm}^{-1}$ in the case of iodine. The coupled basis set, $|Jm_J\rangle$, is constructed from the $|lm_l, sm_s\rangle$ functions by standard methods:

$$|Jm_J\rangle = \sum_{m_l, m_s} c(l s J; m_l m_s m_J) |lm_l, sm_s\rangle. \quad (7)$$

The explicit matrix elements of H_{int} in this basis are given in the Appendix.

Prior to proceeding further, we comment on the applicability of this model. The expansion of the interaction potential in Legendre polynomials, is the standard treatment for electrostatic potentials.²⁹ Restricting values to $L=0$ and $L=2$, implies restricting the description of a central charge distribution to monopole and dipole terms, and considering their interactions with the surrounding electric potential and gradient of the electric potential, respectively. No polarization of the halogen charge distribution is assumed. The expansion is therefore clearly valid for large separations, for $R \gg r$. The expansion is also valid at short range, if the interactions are strictly due to repulsion between charge distributions, and configuration interactions or electron exchange can be ignored. These requirements may be expected to be adequate in the description of the open-shell-closed-shell, X-Rg, since at long range they are characterized by R^{-6} dispersion terms, and at short range they are characterized by $e-e$ repulsion. This is evident from a comparison of the nearly indistinguishable Xe-Xe (Ref. 30) and Xe-I (Ref. 4) pair potentials, which are shown in Fig. 7(a). (The algebraic relations needed to extract Σ and Π potentials from $X_{1/2}$ and $I_{3/2}$ potentials is given by Becker *et al.*³¹) The present treatment is clearly inadequate in the cases of true bonding, extensive exchange, or charge transfer, in which cases the charge distribution on the central atom is strongly polarized by a given interaction. In short, there are no explicit many-body terms in the potentials used. The test of the adequacy of this electrostatic limit, is very much the aim of this work.

B. Potential energy surfaces

We first consider the potential energy surfaces for an I atom surrounded by an octahedral arrangement of Xe atoms, which corresponds to the symmetry of the substitutional site in fcc lattices. For a perfectly symmetric octahedron, the anisotropic terms in the potential disappear and the first term in Eq. (1) is simply reduced to $6V_0(R)$, in which R represents the I-Rg distance. Thus the equilibrium position of the seven atom system, corresponds to the minimum of V_0 . In the two-valued representation, appropriate for an odd number of elec-

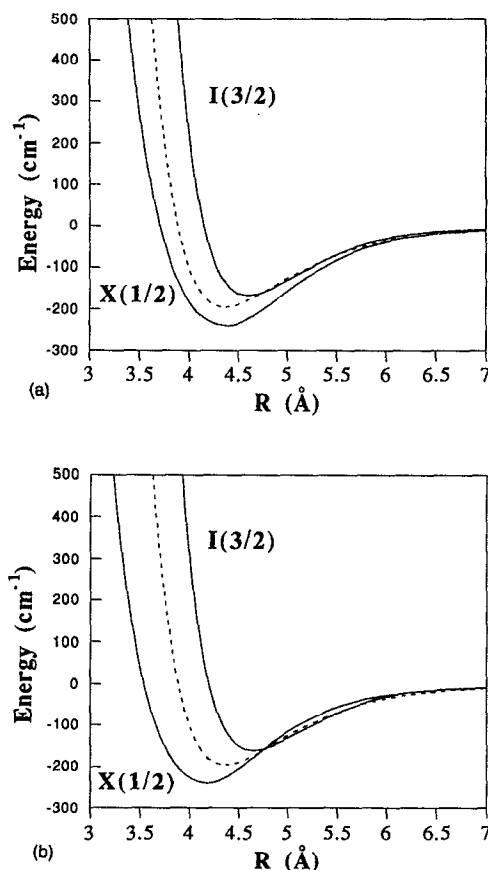


FIG. 7. (a) Pair potentials of Xe-Xe (dashed curve) and Xe-I (solid curves), from Refs. 30 and 4, respectively. (b) Modified pair potentials that yield a satisfactory fit between simulation and experiment in Xe.

trons, in the O_h point group of the heavy atoms, the spin-orbit coupled states belong to the twofold degenerate $E_{1/2}$ and fourfold degenerate $G_{3/2}$ species.³² Vibrations of E_g or T_{2g} modes will produce the Jahn-Teller splitting of the $G_{3/2}$ state, splitting it into $E_{1/2}$ and $E_{3/2}$ spin doublets. This is illustrated in Fig. 8, in which the shape of the potentials along the $\nu_2(E_g)$ vibrational coordinate are considered. In higher dimensions, the splitting results in conical intersections along asymmetric vibrational coordinates.

In the lattice, the I-Rg distance will be determined by Rg-Rg interactions as well. The shape of the Jahn-Teller crossings will then be determined by the particular asymmetric vibrational coordinate considered, and the relative magnitudes of isotropic and anisotropic contributions to the interaction, V_2 and V_0 terms, at the crossing point. The potential energy surfaces that arise for an I atom isolated in a Xe lattice are shown in Fig. 9. For this purpose, a substitutional I atom trapped in an fcc lattice, composed of 108 atoms frozen at their equilibrium geometries, is used. The asymmetric coordinate considered is for in-cage motion of the I atom, along the $[110]$ direction. At the center of the cell, where perfect cubic symmetry is experienced, the doubly degenerate $E_{1/2}$ excited state is separated from the fourfold degenerate $G_{3/2}$ ground state by the spin-orbit splitting, Δ . For any asymmetric motion, the degeneracy of the ground

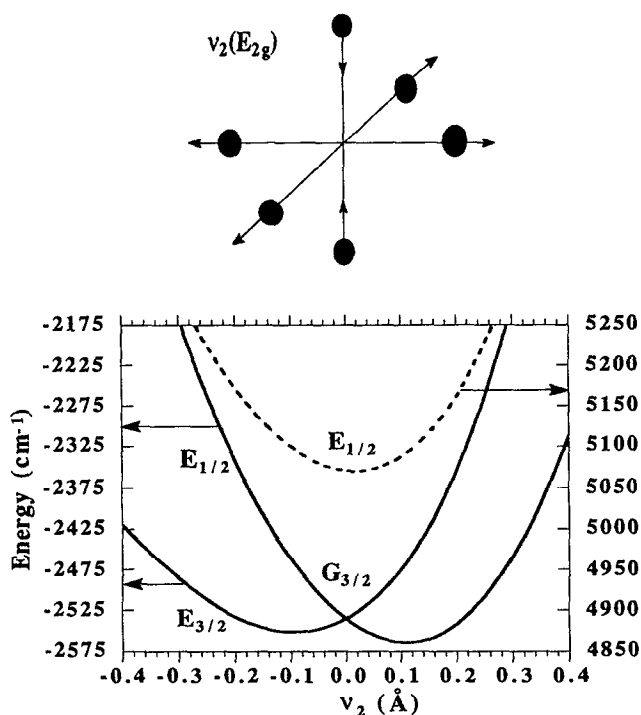


FIG. 8. Potential energy curves for $I(2P)$ surrounded by an octahedral arrangement of Xe atoms. The abscissa corresponds to the amplitude of the ν_2 normal mode, which is indicated above the figure.

states breaks into two states, each a degenerate Kramers pair.

The experimentally observed near IR emission doublets, can formally be assigned to $I^*(2E_{1/2}) \rightarrow I(1E_{1/2}, E_{3/2})$.

C. Spectral simulations

A statistical treatment will be used in the simulation of $I^* \rightarrow I$ spectra. The treatment assumes that the electron on the I atom can perfectly follow the slow dynamics of the heavy

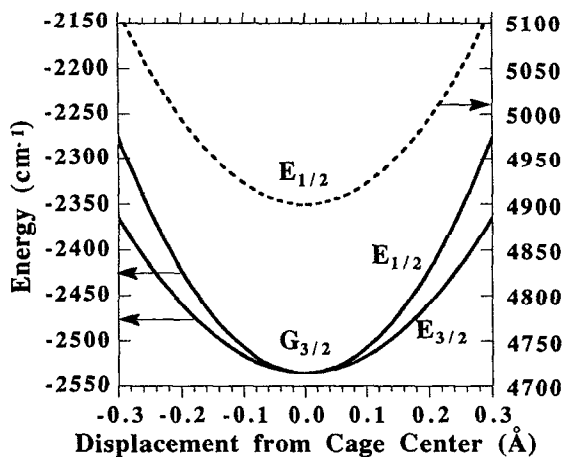


FIG. 9. Potential energy curves for $I(2P)$ isolated in a substitutional site in Xe. The abscissa corresponds to the amplitude of motion of the I atom in the cage, along the 110 direction.

lattice atoms—limit of adiabatic following. Accordingly, for a given configuration of the lattice the energy of the system is given by the eigenvalues of the interaction Hamiltonian of Eq. (1). The formulation further assumes classical statistics for the heavy atoms.³³ This assumption can be justified based on the consideration that although at cryogenic temperatures, the system is in the high temperature limit with respect to all lattice modes, i.e., the thermal energy $\beta^{-1} = k_B T$ is large compared to the energy of motion on a given surface within the de Broglie wavelength $\hbar/(\mu k_B T)^{1/2}$ of the heavy atoms.^{33,34} In the present, for all R_i (but not r)

$$\beta \left(\frac{\hbar}{(\mu k_B T)^{1/2}} \nabla_{\{R_i\}} H_{\text{int}} \right) \ll 1 \quad (8)$$

which is found to be ~ 0.1 at the lowest temperatures of the present measurements (15 K). Thermal distributions in positions of the classical particles can then be generated by standard methods. We note, however, that at cryogenic temperatures the zero-point amplitude of the lattice makes a significant contribution to the position distribution. To take this quantum effect into account, classical distributions at scaled temperatures,³⁵ T' , are generated:

$$T = \frac{\hbar \omega}{2k_B} \left[\tanh \left(\frac{\hbar \omega}{2k_B T} \right) \right]^{-1}, \quad (9)$$

in which ω is identified with the Debye frequency of the solid; $\omega_D = 45 \text{ cm}^{-1}$ and 50 cm^{-1} for Xe and Kr, respectively.³⁶ Thus the experimental temperatures of 17, 35, and 110 K in Xe are scaled up to 33, 45, and 113 K, while those in Kr, 35 and 65 K, are scaled up to 46 and 71 K, respectively.

For a given realization of a configuration in spatial coordinates, three eigenstates arise. The spectral distribution of emission, from state III to I, is given by the multidimensional classical reflection expression:³⁷

$$I_{\text{III} \rightarrow \text{I}}(\omega) \propto Z^{-1} \int e^{-\beta V_{\text{III}}(r; R_1, R_2, \dots, R_n)} |\mu_{\text{III}, \text{I}}|^2 \omega^3 \delta[(V_{\text{III}} - V_{\text{I}})/\hbar - \omega] \Pi_i d^3 R. \quad (10)$$

Z is the classical partition function on the E_{III} surface, where E_i are the three eigenstates which depend explicitly on r , and R_i ; $|\mu_{ij}|$ is the transition dipole moment which in principle depends on all coordinates; the integration is over all classical coordinates. The expression has a simple insight, namely, the emission spectrum represents transitions between eigenstates, weighted by the probability of a configuration on the upper state. A subtlety arises in the evaluation of Eq. (10) which implies an integration over spatial configurations while the energy conserving Dirac delta function is energy normalized.³³ To obtain a space normalized delta function in the integrand, transformation of variables is necessary. Designating a given lattice configuration by the set of position vectors; $Q = \{R_i\}$, and using the properties of delta functions:

$$\delta[(V_{\text{III}} - V_{\text{I}})/\hbar - \omega] = \sum_j \frac{\delta[Q - Q_j]}{|\nabla(V_{\text{III}} - V_{\text{I}})|_{Q_j}}. \quad (11)$$

This replaces the delta function in Eq. (10). The denominator in Eq. (11), the gradient of the difference potentials for a

given lattice configuration, can be identified as the density of states at the resonance condition $V_{III}-V_I=\hbar\omega$. Thus, for a given configuration of the lattice, the transition energy can be calculated from the difference between upper and lower eigenenergies, and the probability of transition at that energy is given by the weight of density of states (and the ω^3 factor, which corresponds to the density of emitted photon states³³).

To evaluate the spectral distribution function we proceed as follows. The Boltzmann weighted initial state configurations are generated by the standard Metropolis algorithm.³⁸ For each configuration the 6×6 Hamiltonian is diagonalized, and the highest eigenenergy is used for the acceptance criterion of a given configuration. For each configuration the transition energies are binned, and weighted by their respective densities of states. The density of states on a given surface, is obtained from the force matrix, using the appropriate eigenvector:

$$|\nabla_{\{R_i\}}V_I| = \left[\sum_i \left(\langle I | \frac{\partial}{\partial R_i} V_{\text{int}} | I \rangle \right)^2 \right]^{1/2} \quad (12)$$

in which $|I\rangle$ is the eigenvector of state I , at a particular classical configuration $\{R_i\}$, and the force matrix is evaluated by taking the gradient of V_{int} . This purely classical treatment leads to singularities where the denominator in Eq. (11) tends to zero (this corresponds to parallel potentials in one dimension). This difficulty was overcome by inclusion of thermal fluctuations to the density of states, replacing the denominator in Eq. (11) by

$$\left(|\nabla_{\{R_i\}}\Delta V|^2 + \frac{\mu(k_B T)^3}{\hbar} \right)^{1/2} \quad (13)$$

The described procedure is rather tedious, and computationally intensive. Learning after some experience that in most of the Monte Carlo realizations, the thermal fluctuations dominate the density of state weighting, we reverted to Eq. (10) for the spectral simulations, i.e., we discovered that the assumption of constant density of states is justifiable. This is strictly true for the spectral distribution within a given emission band, between a pair of electronic states. It is however clear from the potentials of Figs. 8 and 9 that the curvatures of the J - T split states are different and, therefore, the relative intensities of transition to these states should accordingly be different. At the expense of losing this information, we retain the approximate treatment.

The observed 2 orders of magnitude reduction in radiative lifetimes as compared to the isolated atomic transition, is a clear indication that the emission in this case is interaction induced. Accordingly, the spectra were simulated by making different assumptions with respect to the transition dipole. In the first, μ_{ij} is assumed to be a constant, independent of lattice coordinates. In the second, we assume the transition to be proportional to the cage anisotropy

$$\xi = \sum_i R_i; \quad i = 1, \dots, 12.$$

Different powers of ξ , representing different induced poles were tested without a significant change in the simulated spectra. This insensitivity can be attributed to the fact that

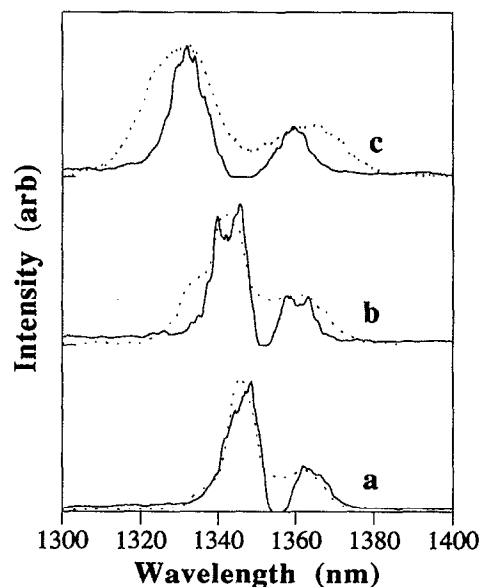


FIG. 10. Comparison between experiment and simulation of $I^* \rightarrow I$ transition in Xe, using unmodified pair interactions. The simulated spectra are normalized, with a 3:1 ratio between the blue and red bands. They are shifted to account for the solid state spin-orbit splitting. The shifts are collected in Table I.

the cage fluctuations are small and symmetrically distributed near the cubic equilibrium configuration, averaging out all odd powers of the anisotropy. Thus, the leading term in the induced poles of the transition is the electric quadrupole, which leads to equal intensities in both emission bands, and to a good approximation can be replaced by a constant probability independent of cage anisotropy.¹² We therefore make the Condon approximation, and use electric quadrupole selection rules in evaluating the spectra.

The simulated spectra for I/Xe , using the I -Xe potentials of Casavecchia *et al.*⁴ and the Xe-Xe potentials of Barker *et al.*,³⁰ are shown in Figs. 10 and 11, together with the experimental data. The simulated spectra reproduce the observed two-band distribution, with zero intensity at the center and a temperature dependent splitting and broadening of the bands. The absence of intensity at the center implies that configurations where eigenstates I and II become degenerate are very rare. This is the configuration of exact cubic symmetry, which upon a casual inspection of the potentials in Fig. 9 may seem highly probable. In effect, all lattice fluctuations split the degenerate pairs, and a perfect cubic symmetry does not occur in 150 000 configurations, with 108 atoms involved in the simulation. Note, the simulations have been shifted to coincide with the observed shift in spin-orbit splitting, Δ , the values of which were collected in Tables I and II. Since Δ is diagonal in the $|Jm_J\rangle$ representation, this shift can be reproduced by simply reducing the value of Δ in H_{int} . Changes in spin-orbit splittings, both positive and negative, are well documented in the literature on matrix isolated atoms, and have been treated in terms of the external heavy atom effect.³⁹ Δ is reduced by $\sim 3\%$ in Xe, and $\sim 5\%$ in Kr. While this effect is nearly constant in Kr, there clearly is a temperature dependence in Xe: the higher the tempera-

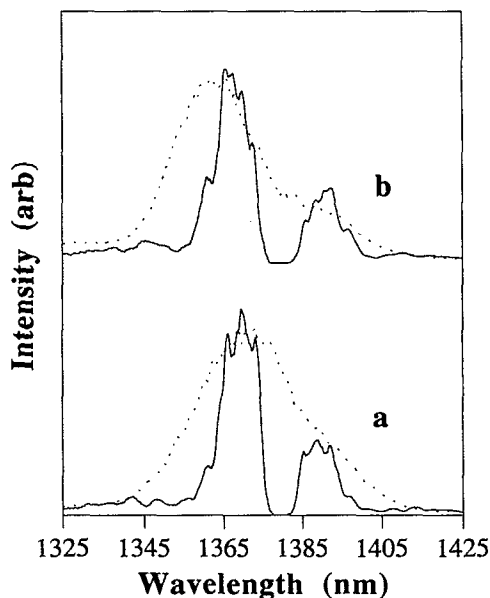


FIG. 11. Comparison between experiment and simulation of $I^* \rightarrow I$ transition in Kr, using unmodified pair interactions. The simulated spectra are normalized and shifted to account for the solid state spin-orbit splitting. The shifts are collected in Table II.

ture the closer is the coupling to that of the free atom. The effect in Xe scales with the density of the solid. Presumably, due to congestion of the trap site, in the case of Kr the bulk density change has little effect on the I-Kr nearest neighbor distance. The $I^* \rightarrow I$ transition has previously been reported in matrices.^{25,26} The excited atomic states in those matrices are accessed by Forster transfer from $I_2(A)$.^{25(a)} Accordingly, the emission intensities, spectral positions, and lifetimes show a strong dependence on sample concentration, and the presence of O_2 . The source of I atoms in those experiments is not well understood, but it is believed that the observed atoms occur near molecular impurities and are perturbed by them. Comparison of our values with those observed in matrices, see Tables I and II, shows that while the Xe data are in acceptable agreement, the Kr data are not. Furthermore, it has also been reported that in Ne instead of two emission bands, three are observed.²⁵ This multiplicity of bands, and the dispersion in the reported transition wavelengths, is an indication that the splittings are effected by local structure. In matrices, the expected heavy atom dependence is observed, the change in Δ is largest in Xe, and smallest in Ne (with opposite sign).²⁵ In the heavy rare gases, Macler *et al.* find a direct correlation between the host polarizability and the red shift in the average spin-orbit splitting. This is in agreement with the temperature dependent shift in Xe which we observe to scale with the bulk polarizability of the solid. It is however surprising in the present to observe a larger change in Δ in Kr than in Xe. We presume that the effect is due to the congestion of the site in crystal Kr, and infer that perhaps in the less dense matrix the site can more easily release the local strain by relaxation.

It is also evident in Fig. 10 that the spectral distributions are significantly narrower in the simulation, and do not re-

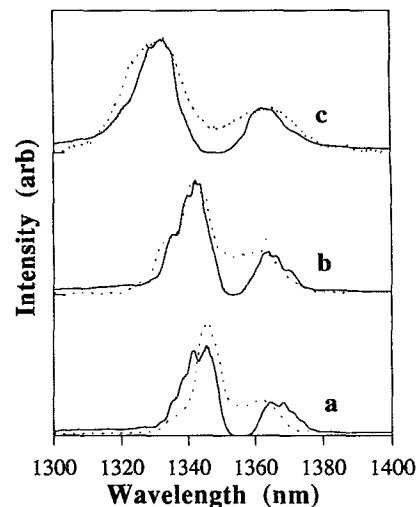


FIG. 12. Comparison between experiment and simulation of $I^* \rightarrow I$ transition in Xe, using modified pair interactions. The simulated bands are relatively normalized by a 3:1 ratio.

produce the details of substructure and its temperature dependence. Minor modifications to the I-Xe potential, within the reported uncertainty of parameters extracted from the scattering data, produces significant changes in the simulated spectra. Although a systematic search for best fit potential parameters was not conducted, after some trials, a rather satisfactory reproduction of the spectrum was obtained. This is shown in Fig. 12 for the case of Xe. The following modifications to the Morse part of the reported pair potentials⁴ were made: the depth of $X_{1/2}$ is adjusted from the reported value of $\epsilon=0.69$ kcal mol⁻¹ to 0.68 kcal mol⁻¹ and that of $I_{3/2}$ is adjusted from $\epsilon=0.48$ kcal mol⁻¹ to 0.46 kcal mol⁻¹; and the equilibrium distance of $X_{1/2}$ is reduced from the reported value of $r_m=4.3-4.2$ Å while that of $I_{3/2}$ is stretched from $r_m=4.6$ Å to 4.65 Å. These modified pair potentials are shown in Fig. 7(b). Note that in the comparison in Fig. 12, the relative intensities of the two bands are adjusted by a 3:1 ratio, as suggested by the experimental data. The temperature dependence of the bands is reproduced and the substructure is evident in the simulation. These features do depend on the choice of potential parameters, however, not in a trivially obvious way.

In summary, experimentally we observe a 3-5 % change in the spin-orbit splitting of I in these solids, by making changes in the Xe-I pair potentials of the same order, the spectral features—splittings and temperature dependent shifts and widths—are reproduced. The variation in Δ is clearly due to exchange interactions with the host atoms, the significance of the variation in the potentials is more difficult to ascertain, since these are within the stated accuracies of the known pair interactions. It can, however, be concluded that at least in the stable trapping sites of the lattice, many-body contributions to the potentials remain less than ~3%, and can be accounted for in the form of effective pair potentials. This result, we feel, justifies the present formalism in treating the anisotropic interactions of the open shell halogens in condensed rare gases.

D. The short-lived emissions

The pair of short-lived emission bands, which are most prominent in the high temperature spectra in Xe, are also ascribed to $I^* \rightarrow I$ transitions. However, the observed large splitting in this case cannot be ascribed to any impacted site of the neutral lattice. For any symmetric trapping site in the lattice in which several nearest neighbor rare gas atoms simultaneously interact with the I atom, the Jahn–Teller (JT) split states cross at the excited state potential minimum, leading to emission bands that nearly overlap. Yet the experimental spectra show a splitting of $\sim 2500 \text{ cm}^{-1}$, with no overlap of bands in the middle. This pattern is only consistent with asymmetric interactions. In particular, for an interaction of $C_{\infty v}$ symmetry, in which, as in the case of diatomic Rg–I, the excited state may emit to the ground Σ and Π surfaces far from their asymptotic convergence. Neutral interactions in the solid cannot yield any configuration in which an isolated diatomic, RgI/Rg, can be imagined which could give the observed splitting. The only possible interpretation is an interaction of the open shell atom with a nearby localized charge. The charge induced dipole interaction lowers the Σ state potential relative to the unaffected Π orientations by $\Delta E = \alpha e^2 / (2R^4)$. Assuming a polarizability of $\alpha = 4 \text{ \AA}^3$ for I, the observed splitting of $\sim 0.29 \text{ eV}$ in Xe would imply $R \sim 3.1 \text{ \AA}$, i.e., a charged nearest neighbor. In the case of Kr the splitting is a factor of 2 smaller, and would therefore imply that the charge center is farther away. For this model to hold, the charged neighbor should be a closed shell species while the I center remains an open shell. Species of the type Rg ^+I is not an acceptable candidate, since it is isoelectronic with interhalogens, and would be expected to be further stabilized by exchange and overlap, leading to the formation of a diatomic with a large multiplicity of states. Negatively charged centers can also be excluded, since in such centers the charge would be expected to localize on I, due to its large electron affinity. The only likely candidate, among the known ionic species in these media, is (RgH) ^+I . Indeed, the IR spectra indicate that upon warmup of irradiated rare gas matrices which are initially doped with hydrogen halides (HX or DX), a strong chromophore involving a charged RgHX center is formed.²³ Given the ionization potentials of the constituent atoms, it can be surmised that the positive charge mainly resides on Xe in (XeH) ^+I , while it should be mainly on H in the case of (KrH) ^+I . Thus if the geometry of such a system is nearly linear H–Rg–I, then the difference between splittings in Kr and Xe can be rationalized.

The (RgH) ^+X center could also explain results of electron spin resonance (ESR) studies in these solids.⁴⁰ Systematic studies in search of ESR spectra of halogens in rare gas solids had failed, leading to the conclusion that interactions with the lattice lead to strong relaxation of the J states, broadening the resonances beyond recognition.^{30,41} This is consistent with the strong JT interactions which we have described for neutral I. In effect, coupling to the lattice phonons destroys the goodness of the total angular momentum quantum numbers. The first exception to these observations were ESR studies of irradiated HI/Xe solids, in which the I hyperfine resonances were found.⁴² This had been in-

terpreted as arising from destruction of the cubic symmetry of the isolation site by the nearby H photofragment. Under the conditions of the experiments, it is doubtful that the H atoms remain trapped in the photolyzed cage, moreover, we believe that a simple cage distortion could not establish a strong quantization axis, to overcome spin-lattice relaxation processes. On the other hand, a quantization axis should be established by the presence of nearest neighbor, closed-shell, charged species. Subsequent to the observation of the ESR spectrum of I, Br atoms were also found in rare gases prepared by passing Br $_2$ /H $_2$ /Ar over a hot filament.⁴³ These were also interpreted by assuming an axial symmetry of the distorted site, arising from H+Br $_2$ reactions. Under the conditions of the ESR experiments, as in the present, charged RgHX $^+$ centers are quite likely, and should be considered closely in the interpretation of the data.

V. CONCLUSIONS

The spectroscopy of spin–orbit transitions of atomic iodine isolated in crystalline Kr and Xe, was presented and used to test the construct of many-body potentials of an open shell system based on known pair interactions. Proper accounting of the nonadditivity of potentials arising from the angular anisotropy of interactions was treated in the electrostatic limit of nonpolarizable charge distributions. Satisfactory agreement between experiment and simulation is only obtained after slight modification, within 3%, of the pair interaction parameters. This test case is somewhat limiting, it involves an open shell atom in a high symmetry site of the lattice in which it fits. Nevertheless, it can be concluded that, many-body contributions to interactions in this case are comparable to those encountered in the closed shell rare gas solids.³⁰ The transitions considered involve spin-coupled orbitally degenerate states, which in the lattice are subject to strong Jahn–Teller instability. Despite the quantum mechanical nature of these interactions, since at the cryogenic temperatures of the solid the system can be regarded to be in the adiabatic following limit, a rather direct method for the spectral simulations is possible. The method involves a classical statistical treatment of the lattice configurations, via a Monte Carlo sampling of the eigenstates of the system. The method is greatly simplified by neglecting the computation of density of states at each configuration, an approximation which is generally valid when the gradient potential surface difference is small compared to kT/λ , where λ is the de Broglie wavelength of the constituent atoms. These conclusions have recently been verified in the case of the two electron system, O(1S) \rightarrow O(1D) transitions in crystalline Kr and Xe.¹²

In addition to the main atomic emission, a second pair of emission bands is observed in these solids. These short-lived emissions are assigned to I atoms with a nearest neighbor, closed shell ion, which is identified as RgH $^+$. It is also suggested that this center may be responsible for the ESR spectra of halogens in rare gas solids. Irradiation of halogen doped rare gas solids leads to delocalized charges, which can separate and form a variety of ionic centers. This consideration is particularly severe in the case of heavy rare gases, and is the main complication in studies of photodissociation

studies of hydrogen halides. Some of the experimental findings in this regard, in particular, regarding the HI/Xe system, were also presented.

ACKNOWLEDGMENTS

This research was supported by the U.S. Air Force Phillips Laboratory under Contract No. S04611-90-K-0035; and in part by the University of California Irvine through an allocation of computer resources. Discussions with H. Kunttu, and his contributions by providing IR data prior to publication are gratefully acknowledged.

APPENDIX

In the $|lm\rangle$ basis set, in the absence of spin-orbit coupling, the V_{X-Rg} elements of the 3×3 matrix are given in Cartesian coordinates as

$$V_{0,0} = \sum_k \left(V_0 + \frac{1}{5} \frac{(3z^2 - r^2)}{r^2} V_2 \right),$$

$$V_{1,1} = \sum_k \left(V_0 - \frac{1}{10} \frac{(3z^2 - r^2)}{r^2} V_2 \right),$$

$$V_{1,0} = \sum_k \left(-\frac{3zx}{5\sqrt{2}r^2} + \frac{3izy}{5\sqrt{2}r^2} \right) V_2,$$

$$V_{1,-1} = \sum_k \left(\frac{3(y^2 - x^2)}{10r^2} + \frac{3ixy}{5r^2} \right) V_2,$$

and

$$V_{-1,-1} = V_{1,1}, \quad V_{1,-1} = V_{-1,1}^*,$$

$$V_{1,0} = V_{0,1}^* = -V_{0,-1} = -V_{-1,0}^*,$$

in which the summation over k is over the rare gas atoms, and the coordinates are the rare gas position components as measured from the halogen core origin.

In the $|Jm_J\rangle$ basis set, the matrix elements including spin orbit coupling are given in Eq. (A1) in terms of the above elements:

$ 1/2, 1/2\rangle$	$ 1/2, -1/2\rangle$	$ 3/2, 1/2\rangle$	$ 3/2, -1/2\rangle$	$ 3/2, 3/2\rangle$	$ 3/2, -3/2\rangle$
$\frac{2}{3} V_{11} + \frac{1}{3} V_{00} + \frac{2}{3} \Delta$		$(\sqrt{2}/3) V_{11} - (\sqrt{2}/3) V_{00}$	$\frac{2}{3} V_{10} - \frac{1}{3} V_{0-1}$	$-\sqrt{\frac{1}{3}} V_{01}$	$\sqrt{\frac{2}{3}} V_{1-1}$
	$\frac{2}{3} V_{11} + \frac{1}{3} V_{00} + \frac{2}{3} \Delta$	$\frac{1}{3} V_{01} - \frac{2}{3} V_{0-1}$	$(\sqrt{2}/3) V_{00} - (\sqrt{2}/3) V_{-1-1}$	$-\sqrt{\frac{2}{3}} V_{-11}$	$\sqrt{\frac{1}{3}} V_{0-1}$
		$\frac{2}{3} V_{00} + \frac{1}{3} V_{11} - \frac{1}{3} \Delta$		$\sqrt{\frac{2}{3}} V_{01}$	$\sqrt{\frac{1}{3}} V_{1-1}$
			$\frac{2}{3} V_{00} + \frac{1}{3} V_{11} - \frac{1}{3} \Delta$	$\sqrt{\frac{1}{3}} V_{-11}$	$\sqrt{\frac{2}{3}} V_{0-1}$
				$V_{11} - \frac{1}{3} \Delta$	
					(A1)

¹ See, for example, W. E. Baylis, *J. Phys. B* **10**, L477 (1977); *J. Chem. Phys.* **51**, 2665 (1969).

² R. M. Whitnell and K. R. Wilson, in *Reviews of Computational Chemistry, Vol. IV*, edited by K. B. Lipkowitz and D. B. Boyd (VCH, New York, 1984), pp. 67-184.

³ I. H. Gersonde and H. Gabriel, *J. Chem. Phys.* **98**, 2094 (1993).

⁴ P. Casavecchia, G. He, R. K. Sparks, and Y. T. Lee, *J. Chem. Phys.* **77**, 1878 (1982).

⁵ K. Tamagake, D. W. Setser, and J. H. Kolts, *J. Chem. Phys.* **74**, 4286 (1981).

⁶ E. E. Nikitin, *J. Chem. Phys.* **43**, 744 (1965).

⁷ R. H. G. Reid and A. Dalgarno, *Phys. Rev. Lett.* **22**, 1029 (1969).

⁸ F. H. Mies, *Phys. Rev. A* **7**, 942 (1973); **7**, 957 (1973).

⁹ V. Aquilanti and G. Grossi, *J. Chem. Phys.* **73**, 1165 (1980).

¹⁰ L. C. Balling and J. J. Wright, *J. Chem. Phys.* **79**, 2941 (1983).

¹¹ J. A. Boatz and M. E. Fajardo, *J. Chem. Phys.* (to be published).

¹² A. V. Danilychev and V. A. Apkarian, *J. Chem. Phys.* **100**, 5556 (1994).

¹³ R. Alimi, R. B. Gerber, and V. A. Apkarian, *J. Chem. Phys.* **89**, 174 (1988).

¹⁴ W. G. Lawrence, F. Okada, and V. A. Apkarian, *Chem. Phys. Lett.* **150**, 339 (1988).

¹⁵ W. G. Lawrence, Ph. D. thesis, University of California, Irvine, 1991.

¹⁶ H. Kunttu, J. Seetula, M. Rasanen, and V. A. Apkarian, *J. Chem. Phys.* **96**, 5630 (1992).

¹⁷ M. Rasanen, J. Seetula, and H. Kunttu, *J. Chem. Phys.* **98**, 3914 (1993).

¹⁸ W. G. Lawrence and V. A. Apkarian, *J. Chem. Phys.* **97**, 2224 (1992).

¹⁹ V. A. Apkarian, in *Proceedings of the International Conference on Lasers 1989*, edited by D. G. Harris and T. M. Shay (STS, McLean, Virginia, 1990), p. 121.

²⁰ H. Kunz, J. G. McCaffery, M. Chergui, R. Schriever, O. Unal, V. Stepanenko, and N. Schwentner, *J. Chem. Phys.* **95**, 1466 (1991).

²¹ M. Kraas and P. Gurtler, *Chem. Phys. Lett.* **174**, 396 (1990).

²² M. E. Fajardo and V. A. Apkarian, *J. Chem. Phys.* **89**, 4102 (1988); **89**, 4124 (1988).

²³ J. Lundell, J. Nieminen, and H. Kunttu, *Chem. Phys. Lett.* **208**, 247 (1993); J. Nieminen, E. Kauppi, J. Lundell, and H. Kunttu, *J. Chem. Phys.* **98**, 8698 (1993); J. Lundell and H. Kunttu, *J. Phys. Chem.* **96**, 9774 (1992).

²⁴ I. Last and T. F. George, *Chem. Phys. Lett.* **177**, 315 (1991); *J. Chem. Phys.* **15**, 8925 (1990).

²⁵ R. Bohling, J. Langen, and U. Schurath, *Chem. Phys.* **130**, 419 (1989).

²⁶ (a) M. Mcler, J-P Nicolai, and M. C. Heaven, *J. Chem. Phys.* **91**, 674

- (1989); (b) M. Macler and M. Heaven, *Chem. Phys.* **151**, 219 (1991).
- ²⁷N. Schwentner, M. E. Fajardo, and V. A. Apkarian, *Chem. Phys. Lett.* **154**, 237 (1989).
- ²⁸A. I. Comes and E. J. Pointek, *Chem. Phys.* **9**, 237 (1975); R. Engleman, B. A. Palmer, and S. J. Avis, *J. Opt. Soc. Am.* **73**, 1585 (1983).
- ²⁹See, for example, W. H. Flygare, *Molecular Structure and Dynamics* (Prentice Hall, New Jersey, 1978).
- ³⁰J. A. Barker, M. L. Klein, and M. V. Bobetic, *IBM J. Res. Dev.* **20**, 222 (1976); also in *Inert Gases*, Vol. 34 of Springer Series in Chemical Physics edited by M. L. Klein (Springer, New York, 1984).
- ³¹C. H. Becker, P. Casavecchia, Y. T. Lee, R. E. Olson, and W. A. Lester, *J. Chem. Phys.* **70**, 5477 (1979).
- ³²G. Herzberg, *Electronic Spectra and Electronic Structure of Polyatomic Molecules* (Van Nostrand Reinhold, New York, 1966).
- ³³M. Lax, *J. Chem. Phys.* **20**, 1752 (1952).
- ³⁴R. Kubo and Y. Toyozawa, *Prog. Theor. Phys.* **13**, 160 (1955).
- ³⁵J. P. Bergsma, P. H. Berens, K. R. Wilson, D. F. Fredkin, and E. Heller, *J. Phys. Chem.* **88**, 612 (1984).
- ³⁶C. Kittel, *Introduction to Solid State Physics, 5th Ed.* (Wiley, New York, 1976).
- ³⁷See, for example, E. J. Heller, *J. Chem. Phys.* **68**, 2066 (1978); E. A. Gislason, *ibid.* **58**, 3702 (1973).
- ³⁸N. Metropolis, A. W. Rosenbluth, M. N. Rosenbluth, A. H. Teller, and E. Teller, *J. Chem. Phys.* **21**, 1087 (1953).
- ³⁹R. Pellow and M. Vala, *J. Chem. Phys.* **90**, 5612 (1989).
- ⁴⁰W. Weltner, *Magnetic Atoms and Molecules* (Dover, New York, 1983), p. 29.
- ⁴¹C. K. Jen, S. N. Foner, E. L. Cochran, and V. A. Bowers, *Phys. Rev.* **112**, 1169 (1958).
- ⁴²M. Iwasaki, K. Toriyama, and H. Muto, *J. Chem. Phys.* **71**, 2853 (1979).
- ⁴³S. V. Bhat and W. Weltner *J. Chem. Phys.* **73**, 1498 (1980).